Journal of Manufacturing Processes 107 (2023) 320–332

Contents lists available at ScienceDirect

Journal of Manufacturing Processes

journal homepage: www.elsevier.com/locate/manpro

Thermo-capillary-gravity bidirectional modelling for evaluation and design of wire-based directed energy deposition additive manufacturing

Alireza M. Haghighi, Jialuo Ding, Yongle Sun *, Chong Wang, Stewart Williams

Welding and Additive Manufacturing Centre, Cranfield University, Cranfield MK43 0AL, UK

ARTICLE INFO

Keywords:
Directed energy deposition
Wire arc additive manufacturing
Analytical model
Bead geometry
Process parameter

ABSTRACT

Wire-based directed energy deposition (w-DED) is an additive manufacturing process well-suited for building large-scale structural components. Deposit bead geometry and its relation to process parameters is a vital aspect of a w-DED process, which is crucial for preventing defects and minimising material waste. In this study, a thermo-capillary-gravity bidirectional analytical model is developed based on the fundamental governing physics, enabling fast predictions of both w-DED bead geometries and process parameters. A novel method is also proposed to determine the power transfer efficiency and wire melting efficiency defined in the model. In the forward modelling, deposit bead geometries, such as layer height and width, can be predicted for given process parameters and material properties. In the reverse modelling, the outputs of the model are process parameters, including heat source power and travel speed, to achieve the deposit bead geometries as required for a given application. This bidirectional modelling approach is applicable to different w-DED processes, and it has been validated for the deposition of steel walls using plasma transferred arc and cold wire gas metal arc processes. The developed bidirectional analytical model could be used as an efficient and reliable tool for w-DED process evaluation and design.

1. Introduction

Additive manufacturing (AM) is an emerging disruptive technology possessing the capability of manufacturing complex parts for a broad range of applications. Directed energy deposition (DED) is an AM process used to deposit materials by employing a directed thermal energy source, and it can be categorised based on the type of energy source used, such as laser beam, electron beam, and electric arc [1,2]. Different metal AM processes can also be distinguished by the adopted form of feedstock, including powder, wire and sheet [3]. Powder-based AM processes can achieve high resolution [3], but they have limitations regarding size of part, rate of deposition, and cost of equipment and material [4]. The wire-based DED (w-DED) is an AM process where wire is used as the feedstock material, and it is effective and efficient for building metallic parts. A typical w-DED process uses gas metal arc (GMA), gas tungsten arc (GTA), or plasma transferred arc (PTA) as the energy source [4–7]. Most of these w-DED process variants are capable of manufacturing large-scale structural components with high deposition rate and reduced material waste [8–12].

Control of the deposit bead geometry through optimising the process parameters is crucial for assuring the quality of the w-DED built parts. If the actual bead geometries are different from those assumed in path planning, deposit defects are likely to occur. The shape and dimension of the deposit bead are determined by the interaction between the w-DED energy and material; the major influential factors for the interaction include the process parameters, material properties, and inter-layer temperature [13]. Accurate prediction of bead geometry helps guarantee or enhance the quality of the final product through lowering the likelihood of defects. It also helps reduce material waste, as it provides better guidance for path planning and maximum use of the material deposited. This is particularly beneficial for large parts made of expensive materials, such as Ti-6Al-4V, which is widely used in the aerospace industry to manufacture structural components. Therefore, it is essential to analyse the relationship between bead geometry and its influential factors in order to have better control on deposition under different w-DED conditions.

Previous research on predicting deposit bead geometry can be categorised based on the approach taken. One popular approach is the data-driven regression model. Sarathchandra et al. [14] investigated the effects of arc current, travel speed and stand-off distance on the 304 stainless steel single bead shape, size, and depth of penetration melting

* Corresponding author.
E-mail address: Yongle.Sun@cranfield.ac.uk (Y. Sun).

https://doi.org/10.1016/j.jmapro.2023.09.069
Received 1 June 2023; Received in revised form 17 September 2023; Accepted 27 September 2023
Available online 27 October 2023

Nomenclature

κ	capillary length
σ	surface tension
ρ_m	density at melting temperature
ρ_0	density at room temperature
g	gravitational acceleration
P_0	pressure at origin
P_z	pressure at point z
R_0	radius at origin
R_z	radius at point z
C_0	curvature at origin
C_z	curvature at point z
φ	contact angle
θ_p	penetration angle
A_b	cross-sectional area of bead
A_l	cross-sectional area of layer
A_p	cross-sectional area of penetration melted region
$W_{Max.}$	maximum wall width
W_E	effective wall width
h_l	layer height
h_p	penetration melting height
H_0	enthalpy at room temperature
H_i	enthalpy at inter-layer temperature
$Q_{Nominal}$	nominal power input
Q_t	total transfered power
Q_w	power for melting wire
Q_p	penetration power
I	current
V	voltage
S	travel speed
S_w	wire feed speed
S_{cw}	cold wire feed speed
S_{hw}	hot wire feed speed
D_w	wire diameter
η_w	wire melting efficiency
η	power transfer efficiency
η_p	penetration melting efficiency

by employing multiple regression models for a w-DED process. The results showed that reducing arc current led to a decrease in the width and an increase in the height of the bead. Xia et al. [15] developed a predictive control algorithm based on vision feedback system using passive visual sensor and image processing method to control the layer width. Their results demonstrated satisfactory accuracy and improvement from previous methods utilizing traditional controllers. Mbodj et al. [16] developed a machine-learning regression algorithm for a laser w-DED process to predict the bead geometry of deposited walls. Although the correlation between bead geometries and process parameters can be established using the data-driven method, the rationale behind the established relation is unclear, and a large amount of data is usually required to re-train the model for any new process or material.

Another approach based on thermo-physical numerical simulation is focused on examining the mechanisms that govern the bead geometry. Geng et al. [17] employed finite element (FE) method to investigate the effects of process parameters on deposit bead height and width for single layer deposition, as well as the thermal behaviour and microstructural evolution. According to their results, increasing arc current and travel speed have positive and negative effects on the deposit bead width, respectively. Bock et al. [18] developed an FE model to analyse the transient heat transfer during the wire-based laser metal deposition (LMD) of a 5xxx series aluminium alloy. The agreement between the temperature fields derived from the simulations and those obtained through experiments validated their LMD heat transfer model, which then can be used to characterise the cross-sectional geometries of deposit bead. Bai et al. [9] developed a computational fluid dynamics (CFD) model to investigate the temperature and fluid flow in molten pool and predict the bead geometry of titanium alloy (Ti-6Al-4V) wall deposited using a PTA-based w-DED process. The predicted dimensions of the deposit beads showed good agreement with experimental results, with mean errors of 10.6 % and 9.7 % for the wall width and height, respectively. However, physics-based numerical models usually take long computational time, which makes them unsuitable for real-time process control or automated path planning.

An analytical model has the potential to be more predictive and robust than regression models and more efficient than physics-based numerical models. In 1982, Matsunawa and Ohji [19] developed an analytical model based on surface tension and capillary force equilibrium to determine the shape and curvature of the bead profile in the single-layer deposition of a welding process. Rios et al. [13] adopted this approach and adapted the model for the w-DED process. They developed an analytical model based on thermo-capillary theory, and the prediction accuracy was within ±20% for Ti-6Al-4V wall deposition using pulsed GTA and PTA w-DED processes. However, the gravity was not considered in their model, resulting in low prediction accuracy for high-density materials. Recently, Mohebbi et al. [20] developed a thermo-capillary-gravity model that integrated the Laplace theorem [21], the energy conservation law and the Newton-Raphson numerical solution algorithm [22]. Their model was validated for a GMA process with consideration of the thermal relations and the effect of gravity on the EN 440 G3Si1 steel deposit bead geometry for different inter-layer temperatures and arc torch travel speeds. One key parameter in their model, i.e., penetration melting efficiency, was calibrated using FE simulation of the heat transfer. The model showed good agreement with experimental results, but it is yet to be verified for predicting the bead geometries for a wider variety of materials and processes.

So far, most models can only provide a unidirectional prediction of bead geometry or other attributes of the w-DED process. There are only a few reports of bidirectional models to predict both bead geometries and process parameters, most of which are based on regression models. For example, Kim et al. [23] developed one of the first bidirectional data-driven models to predict weld bead dimensions and process parameters of GMA welding with steel wire, and the errors in most cases were between 20 % and 40 %. Lee et al. [24] developed bidirectional models for predicting process parameters and deposit bead dimensions of a butt weld joint using a combination of multiple regression model and artificial neural network (ANN) with 48 training patterns. The predicted bead dimensions and process parameters showed good agreement with experimental results. Karmuhilan and Sood [25] developed a bidirectional model using an ANN with analysis of variance (ANOVA). The results were analysed using linear regression to predict bead dimensions or welding process parameters. Although many of the prediction results showed good agreement with experimental data, these data-driven models are largely black box and time-consuming to prepare, requiring a large amount of experimental data for training.

An efficient and robust method for investigating the relationships between w-DED process parameters and bead geometries based on fundamental physics is still needed. In this study, a bidirectional analytical model based on the thermo-capillary-gravity theory is developed, which is applicable to different w-DED processes and materials. In comparison with other modelling approaches, this model is efficient and only needs about six cases for calibration, obtaining the results in a few seconds or minutes. We extend the analytical model proposed by Mohebbi et al. [20] for the forward prediction of bead geometries in straight wall deposition using both traditional and

innovative w-DED processes, and furthermore we realise the new backward prediction of process parameters for given bead geometries. The bidirectional analytical model is validated by comparison with the experimental results for ER90S-G steel wall deposition using PTA and cold wire-GMA (CW-GMA) w-DED processes.

2. Model development

2.1. Governing equations

The surface tension and gravity are the two main factors to determine the shape of the deposit bead [9]. By assuming defect-free full penetration of a two-dimensional molten pool and equal surface tension all over a symmetrical bead surface, based on Laplace's theorem [21], the fundamental equilibrium of capillary and gravity pressures between position z on the bead surface and origin point $z = 0$ (Fig. 1) is expressed as follows [19,20]:

$$P_{(z)} - P_0 = \sigma\left(\frac{1}{R_{(z)}} - \frac{1}{R_0}\right) = -\rho_m\, g\, z \tag{1}$$

where σ is surface tension, R is the radius of the bead surface at each point ($\frac{1}{R_{(z)}} = C_{(z)}$, in which $C_{(z)}$ is the curvature at a point z). The curvature at the point z on the surface can be written as [19]:

$$C_{(z)} = \pm\frac{\frac{d^2z}{dx^2}}{\left[1 + \left(\frac{dz}{dx}\right)^2\right]^{3/2}} \tag{2}$$

Capillary length κ is derived from the ratio of the Laplace pressure (σ/κ) to the hydrostatic pressure ($\rho_m\, g\, \kappa$) [21]:

$$\kappa = \sqrt{\frac{\sigma}{\rho_m\, g}} \tag{3}$$

By using Eqs. (2) and (3), the Eq. (1) can be converted to the following form in the order of z [19,20]:

$$0.5\,\kappa^{-2}\, z^2 - C_0\, z + \int C_{(z)}\, dz = 0 \tag{4}$$

In above equation the integral of $C_{(z)}$ with respect to z is:

$$\int C_{(z)}\, dz = \int \frac{\frac{d^2x}{dz^2}}{\left[1 + \left(\frac{dx}{dz}\right)^2\right]^{3/2}}\, dz = \frac{\frac{dx}{dz}}{\sqrt{1 + \left(\frac{dx}{dz}\right)^2}} + d \tag{5}$$

where the constant d is -1, calculated by imposing the boundary condition at the origin, i.e., $\frac{dz}{dx} = 0$, and employing trigonometric relations reading $\frac{dx}{dz} = cot(\theta)$.

So, through the first integral based on z, the final relation for calculating the height of a bead segment is [19,20]:

$$\frac{0.5\,\rho_m\, g\, z^2}{\sigma} - \frac{z}{R_0} + \left(\frac{\frac{dx}{dz}}{\sqrt{1 + \left(\frac{dx}{dz}\right)^2}} - 1\right) = 0 \tag{6}$$

By getting the second integral, the width of a bead segment at any height position from the origin can be calculated via:

$$x = \pm 0.5 \int_0^z \left[\frac{\sqrt{1 + f(z)}}{\sqrt{1 - f(z)}} - \frac{\sqrt{1 - f(z)}}{\sqrt{1 + f(z)}}\right] dz \tag{7}$$

where $f(z)$ is a quadratic equation in the order of z and in the form of the elliptical integral. The second integral from Eq. (6) with respect to z is:

$$x = \pm\frac{1}{\sqrt{\left(\kappa^{-2} + \frac{0.25}{R_0^2}\right)}} \left\{ \begin{array}{l} \left(2 + \frac{0.5\kappa^2}{R_0^2}\right)\left[E\left(cos^{-1}\left(\sqrt{1 - \frac{1}{\sqrt{1 + (tan\psi)^2}}}\right), \sqrt{\frac{\kappa^{-2}}{\kappa^{-2} + \frac{0.25}{R_0^2}}}\right) - E\left(\frac{\pi}{2}, \sqrt{\frac{\kappa^{-2}}{\kappa^{-2} + \frac{0.25}{R_0^2}}}\right)\right] \\ -\left(1 + \frac{0.5\kappa^2}{R_0^2}\right)\left[F\left(cos^{-1}\left(\sqrt{1 - \frac{1}{\sqrt{1 + (tan\psi)^2}}}\right), \sqrt{\frac{\kappa^{-2}}{\kappa^{-2} + \frac{0.25}{R_0^2}}}\right) - F\left(\frac{\pi}{2}, \sqrt{\frac{\kappa^{-2}}{\kappa^{-2} + \frac{0.25}{R_0^2}}}\right)\right] \end{array} \right\} \tag{8}$$

where F and E are elliptic integrals of the first and second kinds, respectively. The bead shape parameters in a two-dimensional cross-section of bead deposition are illustrated in Fig. 1. The elliptic integrals are expressed as:

$$F(\phi, k) = \int_0^{\phi} \frac{1}{\sqrt{1 - k^2 sin^2\beta}} d\beta \tag{9}$$

$$E(\phi, k) = \int_0^{\phi} \sqrt{1 - k^2 sin^2\beta}\, d\beta \tag{10}$$

The cross-sectional areas of the whole bead, the penetration melted region and the deposit layer, as denoted by A_b, A_p and A_l (Fig. 2),

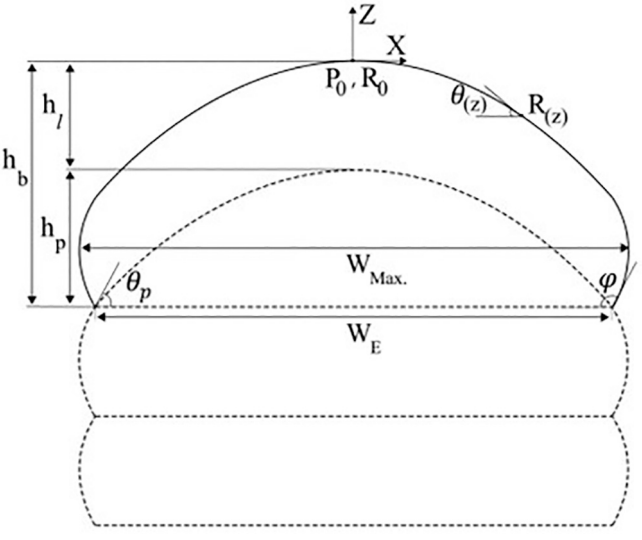

Fig. 1. Geometric variables of the cross-sectional profile of a deposit bead in a straight wall deposited using a single-pass multi-layer w-DED process.

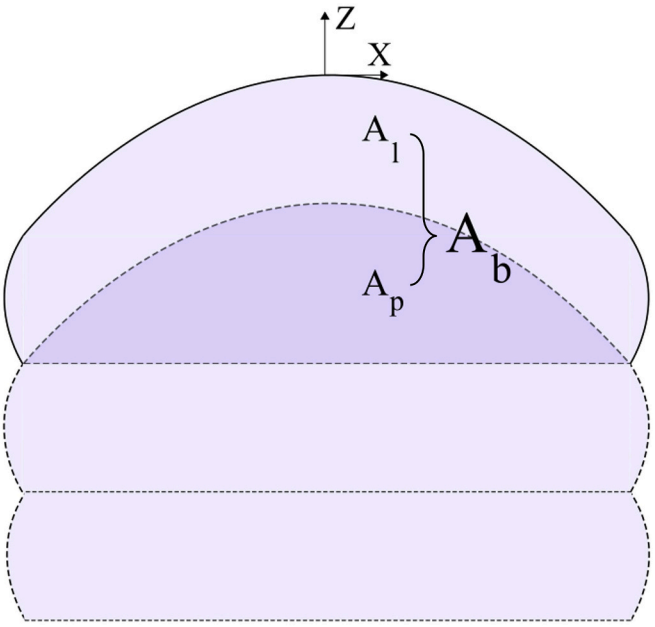

Fig. 2. Cross-sectional areas of deposit layer (A_l), penetration melted region (A_p) and whole bead (A_b) in a straight wall deposited using a single-pass multi-layer w-DED process.

respectively, are calculated by getting the integral from Eq. (8) with respect to z and inserting R_0, θ_p and φ (only two of these three variables are independent) [20]:

$$A_b = -2\int_0^{z_\varphi} x\,dz$$
$$A_p = -2\int_0^{z_{\theta_p}} x\,dz \tag{11}$$
$$A_l = A_b - A_p$$

It should be mentioned that the fusion boundary associated with the penetration melting is assumed to be flat in the model (Fig. 2). The actual fusion boundary could render more complicated shape, but the prediction of the bead surface profile is hardly affected, as long as the penetration molten area is equivalent.

2.1.1. Forward model for predicting bead geometries

In the forward model to predict bead geometries using Eqs. (6) and (8), three unknown variables, i.e., origin curvature R_0, penetration angle θ_p, and contact angle φ (Fig. 1), should be calculated, which require addiontal equations resorting to conservation laws of energy and mass. First, the required power supply for melting the wire in the w-DED process is [20]:

$$Q_w = 0.25\,\pi\,D_w{}^2\,S_w\,\rho_0\,H_0/\eta_w \tag{12}$$

where D_w is the wire diameter, S_w is the wire feed speed, ρ_0 is the density of the material at room temperature and H_0 is the enthalpy difference of the material between the melting temperature and room temperature, i.e.:

$$H_0 = H(T_m) - H(T_0) \tag{13}$$

and η_w is wire melting efficiency, which is the ratio of the power consumed for melting the wire to the power absorbed by the wire. There is a small amount of power, which is usually less than 11 % ($\eta_w > 89\%$), for heat loss to environment, besides the net power consumed for melting the wire.

The penetration power, Q_p, is defined as the remaining power after the supplied power for melting wire, Q_w, is subtracted from the total transferred power, Q_t. Therefore, the penetration power is expressed as [20]:

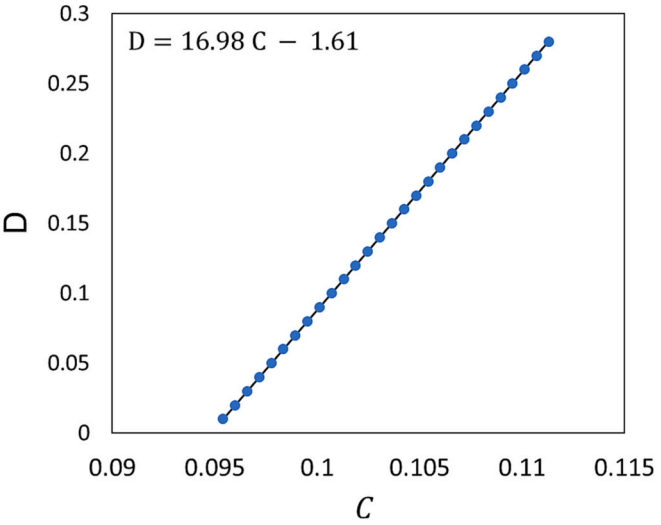

Fig. 4. Relation of variables C and D in the equation of cross-sectional area of penetration melted region for a case of PTA process.

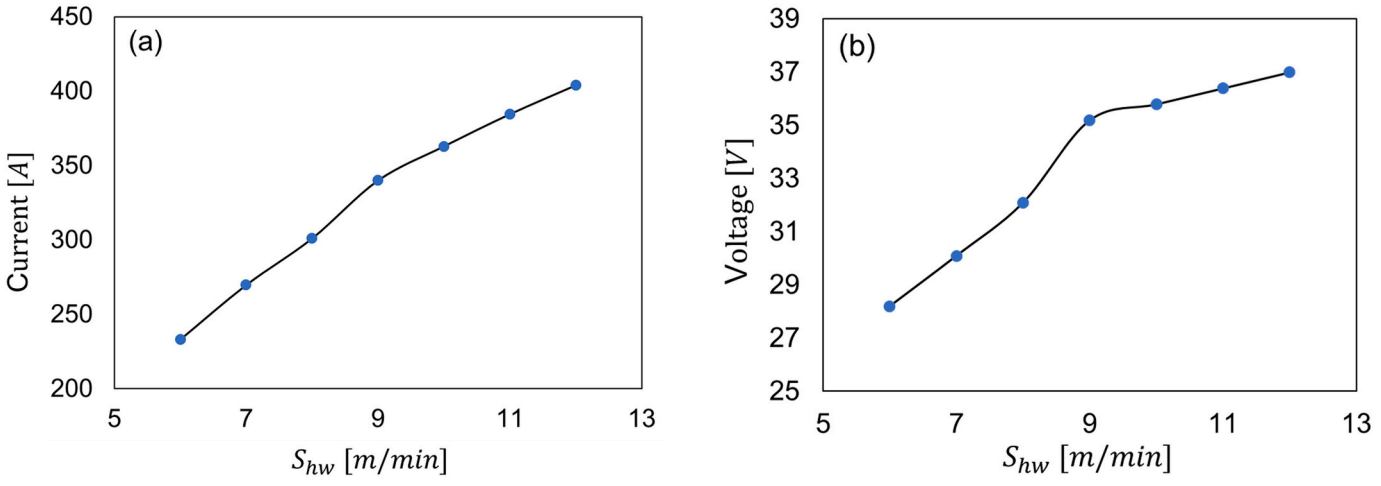

Fig. 3. The variations of arc current (a) and voltage (b) with the hot wire feed speed of the CW-GMA process [26].

Table 1
Power transfer and wire melting efficiencies for 5 cases of PTA process using ER90S-G steel wire

Case	S_w [mm/s]	S [mm/s]	I [A]	V [V]	$W_{Max.}$ [mm]	h_l [mm]	C	D	η	η_W
1	25.0	2.2	184	24	10.5	1.2	0.11	0.19	0.63	0.95
2	24.7	2.0	189	23	10.0	1.4	0.11	0.19	0.62	0.95
3	23.3	2.5	191	25	9.5	1.2	0.10	0.17	0.56	0.93
4	25.0	2.0	206	26	11.0	1.3	0.09	0.17	0.57	0.94
5	30.0	3.0	210	26	9.7	1.1	0.11	0.18	0.62	0.93
Average									0.60	0.94

$$Q_p = Q_t - Q_w = A_p\, H_i\, \rho_m\, S/\eta_p \tag{14}$$

where A_p is the cross-sectional area of the penetration melted region in the previous layer, H_i is the enthalpy difference of the material between melting temperature and inter-layer temperature, ρ_m is the density at melting temperature, S is heat source travel speed and η_p is penetration melting efficiency. The transferred portion of the nominal power supplied to the material is [20]:

$$Q_t = \eta\, Q_{nominal} = \eta\, V\, I \tag{15}$$

where V and I are arc voltage and current, respectively, and η is the power transfer efficiency. When other type of energy source (e.g., laser beam) is employed, the $Q_{nominal}$ can be expressed differently.

Due to mass conservation, the cross-sectional area of the deposit layer, A_l, is calculated by [20]:

$$A_l = 0.25\, S_w\, \pi\, D_w^2/S \tag{16}$$

By using Eqs. (12) and (15), the cross-sectional area of the penetration melted region is [20]:

$$A_p = \frac{\eta_p\left(\eta\, I\, V\; -\; 0.25\,\pi\, D_w^2\, S_w\, \rho_0\, H_0/\eta_w\right)}{H_i\, \rho_m\, S} \tag{17}$$

The cross-sectional area of the whole bead, A_b, is the sum of the cross-sectional areas of the deposit layer and penetration melted region (Fig. 2).

Incorporating the above equations for calculating the cross-sectional areas in Eq. (11), a system of three equations with three unknown variables of R_0, θ_p and φ can be established, viz. [19,20,22]:

$$\begin{cases} A_b = A(R_0, \varphi) \\ A_p = A(R_0, \theta_p) \\ x(R_0, \varphi) = x(R_0, \theta_p) \end{cases} \tag{18}$$

Newton-Raphson iteration method can be employed to solve Eq. (18). After obtaining R_0, θ_p and φ, the height and width of any bead segment can be calculated using Eqs. (6) and (8), respectively.

2.1.2. Reverse model for predicing process parameters

For the reverse model, the bead geometries (e.g. layer height and width) are given as a requirement. First, according to Eqs. (6) and (8), three unknown variables of R_0, θ_p and φ should be determined using a system of three governing equations (similar to the forward model described in Section 2.1.1), which can be solved through Newton-Raphson iteration. The reverse model inputs are the effective wall width W_E (or maximum wall width $W_{Max.}$), layer height h_l and material properties, and then assuming equal width for the penetration melted region $W_{E\theta_p}$ and deposited layer $W_{E\varphi}$, (Fig. 1), we have:

$$\begin{cases} -h_l = z_\varphi - z_{\theta_p} \\ W_{E\varphi} = W_{E\theta_p} \\ W_E = 2\, x(\varphi) \text{ or } W_{Max.} = 2\, x\left(\frac{\pi}{2}\right) \end{cases} \tag{19}$$

After solving Eq. (19), the A_b, A_p and A_l can be calculated by employing Eq. (11) with respect to z and inserting the obtained R_0, θ_p and φ. Here, S_w is assumed to be known for the required deposition rate. It should be also noted that $S_w = S_{cw} + S_{hw}$ for the CW-GMA process. By having A_l, A_p and S_w, based on Eqs. (12), (14) and (16), the S, Q_w and Q_p can be calculated.

The total transferred power to the material can be calculated as:

$$Q_t = Q_p + Q_w \tag{20}$$

Combining Eqs. (15) and (20), we can determine the heat source

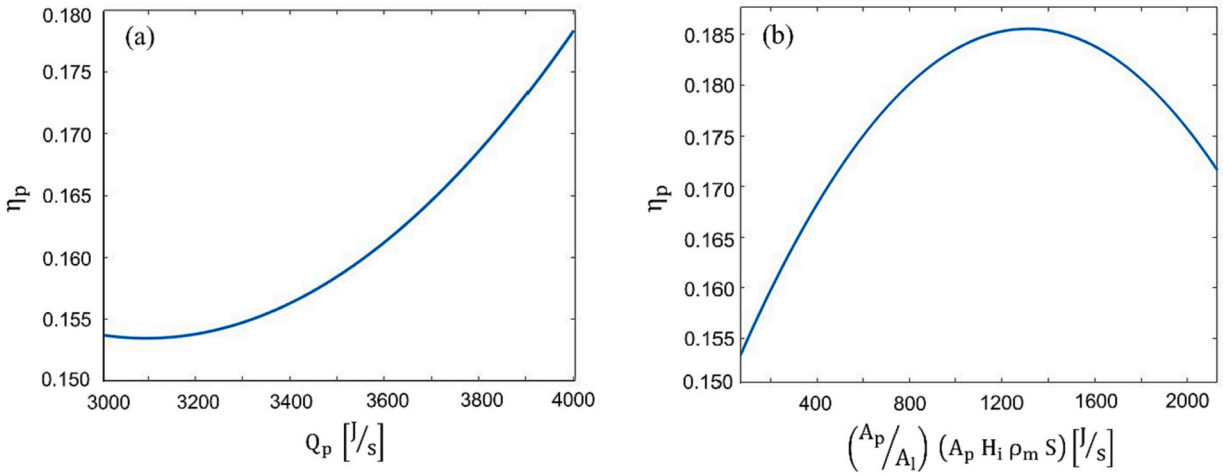

Fig. 5. Calibrated penetration melting efficiency of PTA-based process using ER90S-G steel wire with an inter-layer temperature of 70 °C for forward model (a) and reverse model (b).

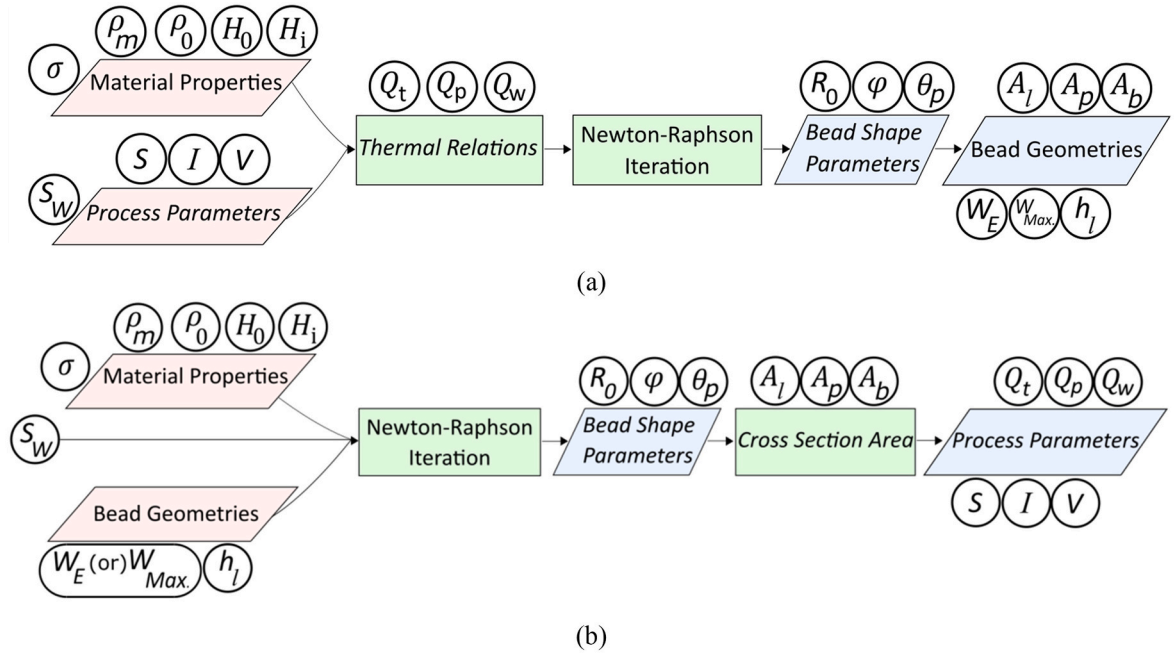

Fig. 6. (a) Flowchart of forward model for prediction of bead geometries; (b) Flowchart of reverse model for prediction of process parameters.

Table 2
Chemical composition of ER90S-G copper-coated steel (Wt%)

C	Cr	Cu	Mn	Mo	P	Si	S	Fe
0.08	2.50	0.12	0.60	1.00	0.01	0.60	0.01	Bal.

power and also the arc and voltage for a arc-based w-DED process. For the PTA process, a linear relation between current and voltage exists for a PTA machine with a fixed torch stand-off distance. For the CW-GMA process, the current and voltage depend on the hot wire feed speed S_{hw}. The following linear relation between the current and voltage for the PTA-based w-DED process was determined by recording the current I [A] and voltage V [V] of separate experimental tests using a 3-axis CNC machine with 8 mm torch stand-off distance:

$$V = 0.07\,I + 11.52 \tag{21}$$

For the CW-GMA process, Fig. 3 shows the nonlinear dependence of the current and voltage on the hot wire feed speed [26]:

2.1.3. Power transfer efficiency and wire melting efficiency

Power transfer efficiency η is a parameter to specify the ratio of the power transferred to the wire, substrate, and previous deposited layers from the energy source [27]. The power transfer efficiency is a critical parameter in the deposition process because a low transfer efficiency could lead to low penetration power that limits travel speed. It was also reported that low transfer efficiency causes the limitation of penetration melting efficiency [28].

In previous research, the power transfer efficiency is usually considered as a constant or to be dependent on a specific process parameter. Sindo Kou [27] reported power transfer efficiency for different welding processes, including PTA, GMAW, gas-tungsten arc welding (GTAW) and submerged arc welding (SAW), and the typical transfer efficiency values fall in the range from 0.5 to 0.7 for PTA and 0.6 to 0.8 for GTAW. Barrionuevo et al. [29] reported a power transfer efficiency ranging 0.8–0.9 for electrode-consuming welding processes (e.g. GMAW and SAW) and about 0.5 for non-consumable electrode processes (e.g. GTAW and PTA).

To the authors' best knowledge, there is no tailored method for the determination of the power transfer efficiency and wire melting efficiency for the w-DED process. This study presents a novel method to determine the two efficiency parameters based on the thermo-capillary-gravity model and experimental data. For this purpose, by categorizing the efficiency parameters of Eq. (17), we have:

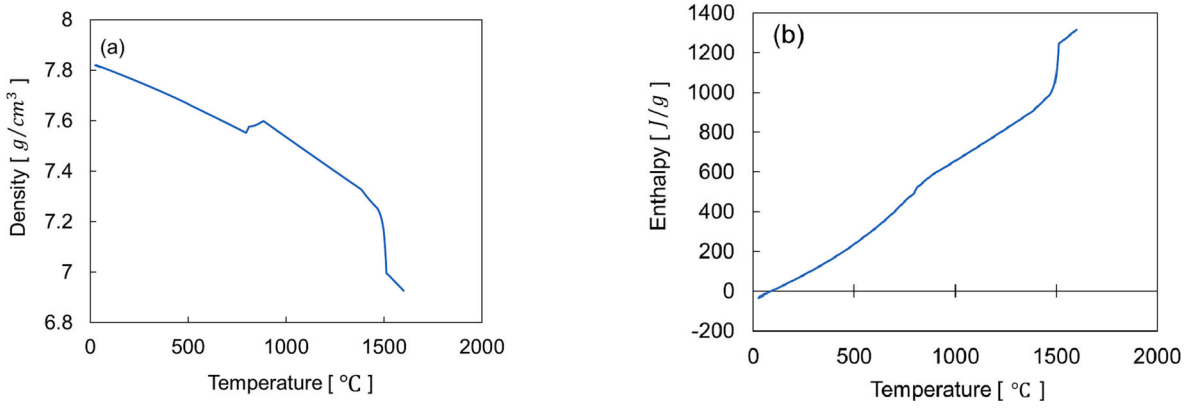

Fig. 7. Density (a) and enthalpy (b) of ER90S-G steel wire versus temperature.

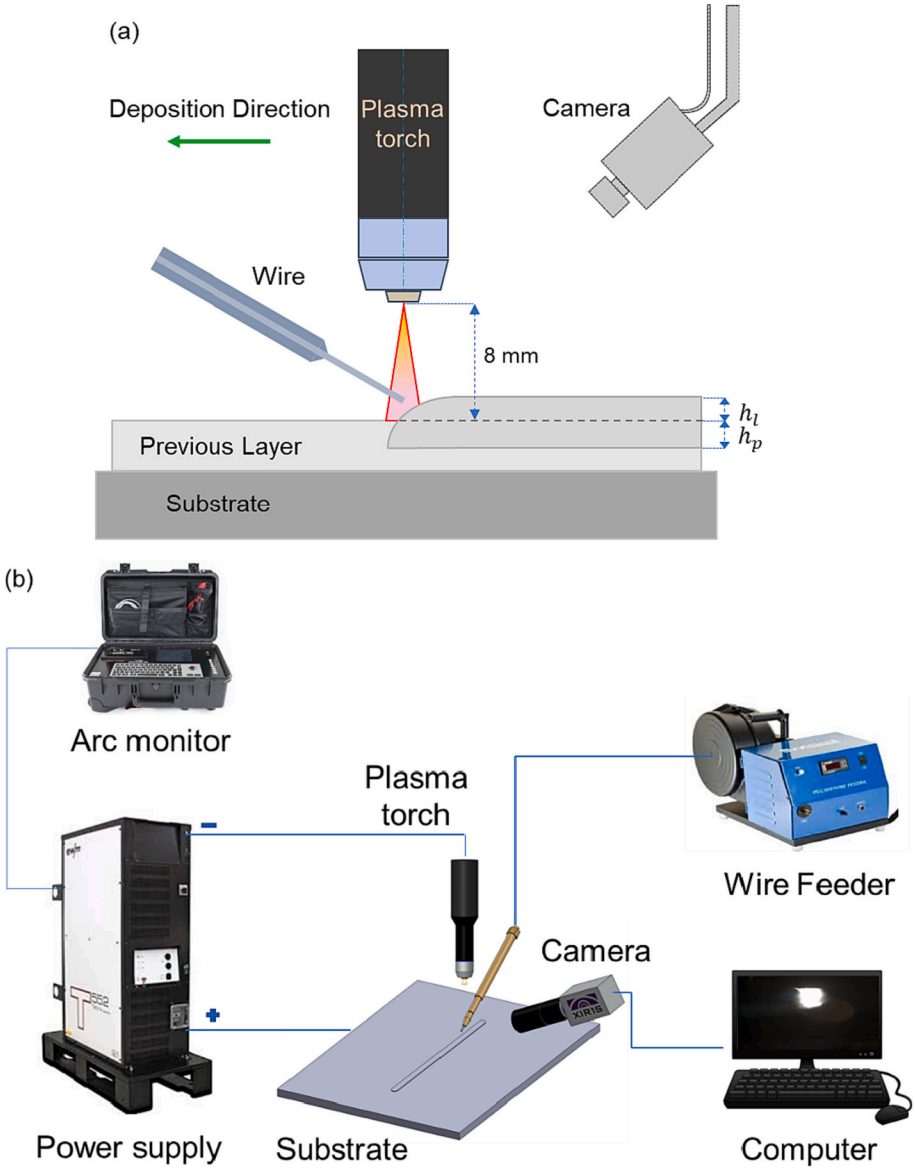

Fig. 8. (a) Schematic configuration of the PTA-based process (side view) for single-pass multi-layer straight wall deposition using ER90S-G steel wire, and illustration of the layer height h_l and penetration melting height h_p; (b) Experimental setup of PTA deposition process and equipment.

$$A_p = \frac{C\,(I\,V) - D\,\left(0.25\,\pi\,D_w^2\,S_W\,\rho_0\,H_0\right)}{H_i\,\rho_m\,S} \tag{22}$$

in which

$$\begin{cases} C = \eta_p\,\eta \\ D = \eta_p/\eta_w \end{cases} \tag{23}$$

For the calculation using Eq. (22) to determine the relation of variables C and D, experimental data of bead geometries and process parameters of a few deposited walls are needed. For each case, the C-D relation is the only unknown in Eq. (22) to be exported from the calibration algorithm. Fig. 4 shows the C-D relation for a case of PTA-based w-DED process using ER90S-G steel wire with 8 mm torch stand-off distance.

Then, using the C-D relation, Eq. (23) and experimental data, we can obtain the efficiencies η and η_w for different combinations of C and D. The outputs are deemed reasonable if the obtained wire melting efficiency is no less than 90 %. The power transfer efficiency and wire melting efficiency of each case can be determined by getting an average of all the results calculated.

By repeating these calculations for 5 cases of the PTA process, the average power transfer efficiency and wire melting efficiency can be obtained. Table 1 shows the calibrated efficiency parameters for the PTA deposition using the ER90S-G steel wire and 3-axis CNC machine with 8 mm torch stand-off distance.

2.1.4. *Penetration melting efficiency*

The penetration melting efficiency is a parameter to define the ratio of the power used to create a molten pool to the power delivered to and absorbed by the workpiece [26]. To enhance the accuracy of the model, the penetration melting efficiency was calibrated after obtaining the power transfer efficiency and wire melting efficiency. For this purpose, the penetration melting efficiency of each case can be calculated using the calibration algorithm and experimental results for about six walls. The following relations were developed based on the influential parameters on the penetration melting efficiency, viz.

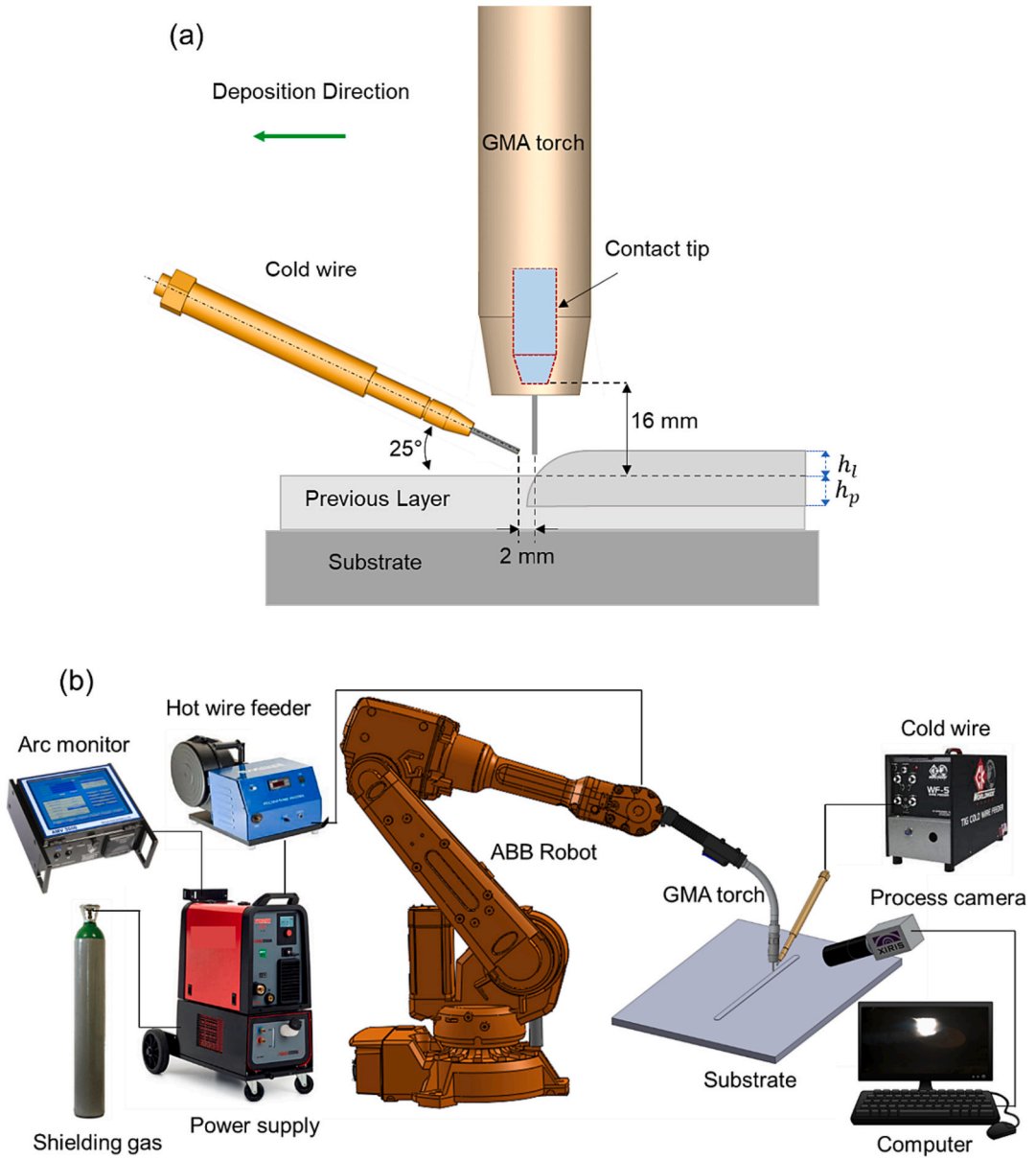

Fig. 9. (a) Schematic configuration of the CW-GMA deposition process with two feed wires, and illustration of layer height h_l and penetration melting height h_p; (b) Experimental setup of CW-GMA deposition process and equipment.

$$\eta_p \begin{cases} Q_p & \text{Forward Model} \\ \left(A_p/A_l\right)\left(A_p\, H_i\, \rho_m\, S\right) & \text{Reverse Model} \end{cases} \tag{24}$$

Then, repeating this procedure for several cases, two fitting curves of the penetration melting efficiency can be established to express the relations in Eq. (24) for the forward and reverse models, respectively, making it possible to predict the penetration melting efficiency for a range of process parameters. Fig. 5a and b show the calibrated penetration melting efficiency using a set of PTA deposition experiments, including five ER90S-G steel single-pass deposited walls with a length of 120–140 *mm* and at least seven layers deposited at an inter-layer temperature of 70 °C for the forward and reverse models, respectively. It is worth mentioning that the accuracy of the calibration method depends on the experimental data set, and the prediction error for the cases out of the process parameter limits could be higher. In this study, the calibration cases were chosen over a wide range of parameters to cover a large regime of the process envelope.

2.2. Solution algorithm

Fig. 6a shows the flowchart of the thermo-capillary-gravity model for forward prediction with inputs of material properties and process parameters and outputs of bead geometries, including layer height h_l, effective wall width W_E and maximum wall width $W_{Max.}$ (Fig. 1). In addition, subsidiary results such as the cross-sectional areas of the deposit layer A_l, the penetration melted region A_p and the whole bead A_b (Fig. 2) can be also obtained. Similar approach for forward modelling was adopted and validated in previous research [20]. The reverse model requires inputs of material properties and bead geometries (two bead shape parameters, i.e. h_l and W_E (or $W_{Max.}$) should be provided), and the model outputs are process parameters, as shown in Fig. 6b. The reverse model also produces subsidiary results such as total transfered power Q_t, power for melting the wire Q_w and penetration power Q_p. Since the number of unknown variables in reverse modelling is more than the number of the governing equations, one process parameter needs to be specified. In practice, the wire feed speed S_w, corresponding to the single

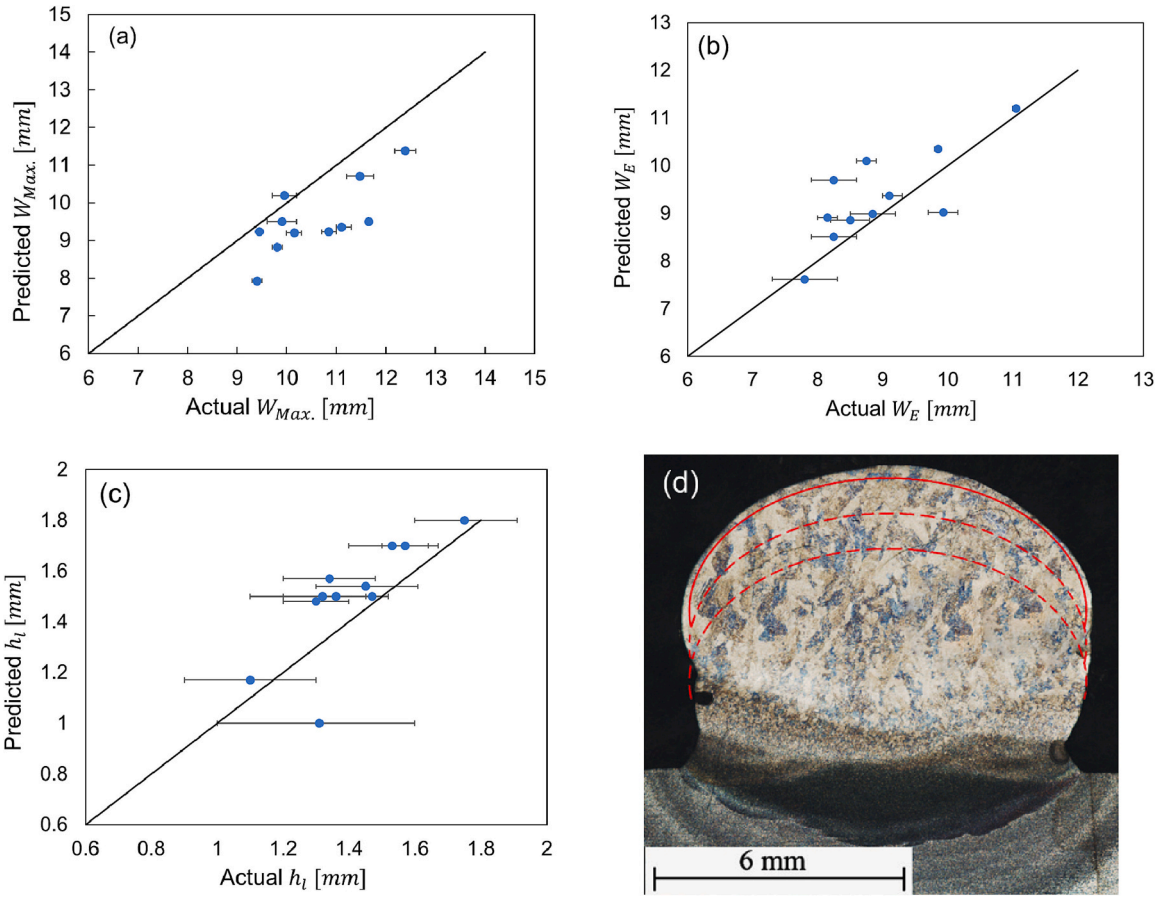

Fig. 10. Comparison of predicted and actual maximum wall width $W_{Max.}$ (a), effective wall width W_E (b) and layer height h_l (c) for PTA samples. The predicted bead shape (red line) for one typical case of PTA deposition using ER90S-G steel wire with an inter-layer temperature of 70 °C is superimposed in the etched macrograph (d). (For interpretation of the references to colour in this figure legend, the reader is referred to the web version of this article.)

wire of the PTA process or both hot and cold wires of the CW-GMA process, is usually directly specified to meet the requirement of deposition rate for a given application. Therefore, the wire feed speed is treated as a given parameter in the reverse model.

3. Validation experiments

The thermo-capillary-gravity model was developed to predict both bead geometries and process parameters for single-pass multi-layer deposited wall. Two different w-DED processes with typical specifications were chosen for the experimental validation of the analytical model in the two prediction directions. The selected two w-DED processes are different in several aspects. For instance, the PTA process produces relatively smooth surface finish with low deposition rate, while the CW-GMA process has a high deposition rate but relatively low resolution. Sufficient cases in each w-DED process were used to validate the forward and reverse models. The deposited wall dimensions were measured after depositing about five layers because the heat transfer in the first a few layers is strongly affected by the substrate geometry and properties, which is beyond the capability of this model. In this section, the experimental setups of the PTA and CW-GMA processes are described.

3.1. PTA-based w-DED process with ER90S-G steel wire

In the PTA deposition experiments, the material used for the wire was copper-coated high-strength low alloy steel (ER90S-G) with a diameter of 1.2 mm, see Table 2 and Fig. 7 for material properties as provided by the manufacturer, while a mild steel was used for the substrate with dimensions of 200 mm × 330 mm × 10 mm. The substrate was cleaned with acetone to remove contamination before deposition and clamped to the worktable.

Fig. 8 shows the experimental setup of a typical PTA-based w-DED process. A 3-axis CNC machine was used to provide the motion of the energy source. The stand-off distance between the PTA torch and substrate (or previous deposited layer) was set to be 8 mm. An arc monitor (AMV 4000) was used to record the arc current and voltage. Also, a CMOS camera (Xiris XVC-100) with properly adjusted distance and view angle was positioned for observation of molten pool and wire droplets. Sixteen defect-free single-pass multi-layer walls were deposited with a wide range of process parameters, and five samples were used for model calibration and the other eleven for model validation. The bead dimensions were measured using a calliper.

3.2. CW-GMA process with ER90S-G steel wire

The CW-GMA process is an innovative process for DED AM, in which both hot wire (electrode) and cold wire (non-electrode) are fed simultaneously to the molten pool to increase the deposition rate [26]. For the complicated wire feeding in the CW-GMA process, the ER90S-G steel was used for both the cold and hot wires with a 1.2 mm diameter and a 2 mm distance between the two wires. A grinded mild steel plate with dimensions of 300 × 200 × 12.7 mm was clamped to the worktable as the substrate for the deposition. Shielding gas consisting of 92 % argon and 8 % CO_2 was used with a flow rate of 20 L/*min* during the deposition process.

Twenty-six walls with at least ten layers for each sample, covering a wide range of process parameters and a large regime of the process

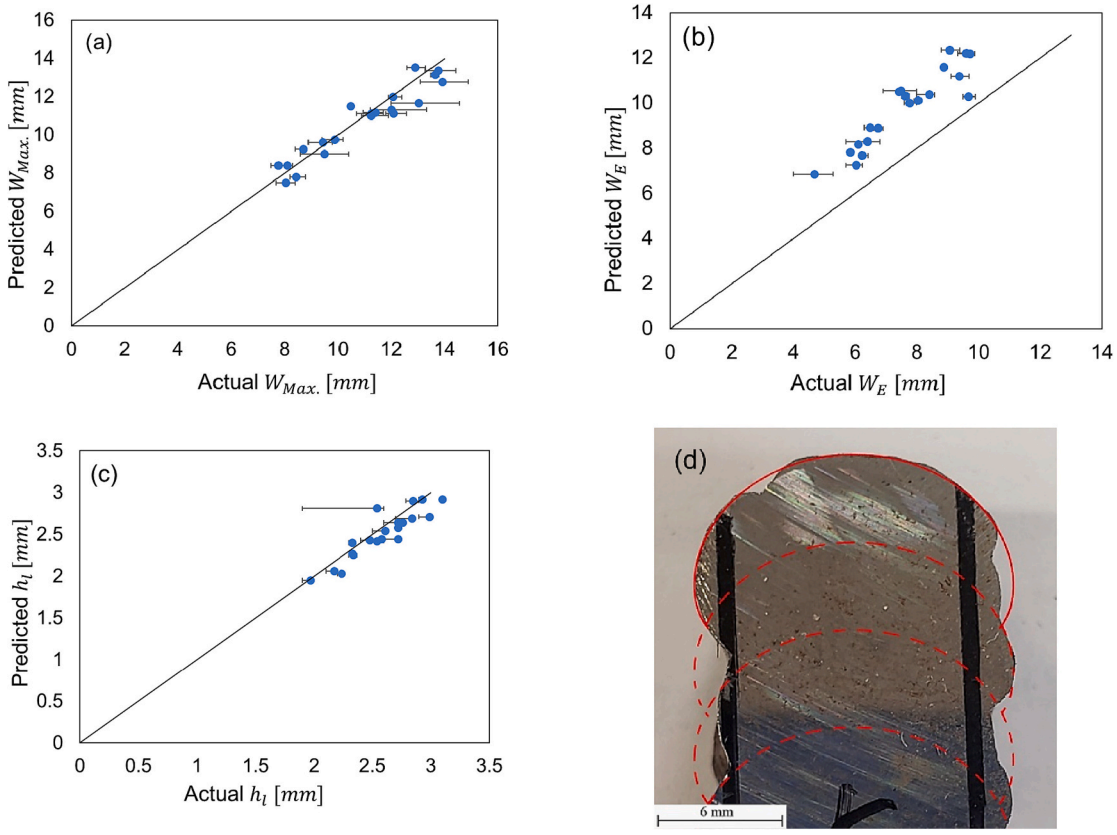

Fig. 11. Comparison of predicted and actual maximum wall width $W_{Max.}$ (a), effective wall width W_E (b) and layer height h_l (c) for CW-GMA samples. The predicted bead shape (red line) is superimposed in the cross-sectional macrograph for one typical case of CW-GMA deposition process (d). (For interpretation of the references to colour in this figure legend, the reader is referred to the web version of this article.)

envelope, were deposited by a 6-axis ABB robot, and the bead geometries of each sample were measured using a caliper. Six samples were used to calibrate the penetration melting efficiency using Eq. (24), while the other twenty samples were used for model validation. Fig. 9 shows the schematics and experimental setup of the CW-GMA process.

4. Results and discussion

4.1. Bead geometries predictions

4.1.1. Predicted PTA bead geometries

Predictions of the bead geometries, i.e. $W_{Max.}$, W_E and h_l, for the PTA process using ER90S-G steel wire for eleven cases of deposited walls are shown in Fig. 10a–c. The samples were cut in three different cross sections along the length of the deposited wall (error bars indicate extreme values), and the average measured results are compared with the model predictions. Each data point represents a comparison of predicted and measured results. The solid straight line indicates the ideal agreement that the predicted and measured data were identical. So, the vertical distance of each point from the nominal straight line indicates the magnitude of error for that case. In general, the model provides an accurate prediction, of which the average percentage error of the predicted $W_{Max.}$, W_E and h_l are 9.8 %, 6.0 % and 9.6 %, respectively, with average calculation time of 80 s, and the highest error is 18 % in one case. The prediction accuracy of the analytical model is similar to or even better than the accuracy of complicated physics-based numerical simulations. For instance, Bai et al. [9] found 10.6 % and 9.7 % prediction errors by their CFD simulation model for the width and height of the deposited layer, respectively, in a PTA process. Fig. 10d shows the comparison of the predicted bead shape and the actual etched cross-sectional profile of the deposited wall for one typical case, and a good agreement is found again.

4.1.2. Predicted CW-GMA bead geometries

Fig. 11a–c shows the comparison between the bead geometries obtained by the model and experiments for the CW-GMA process. Fig. 11d shows the predicted bead shape, plotted on the imaged cross section of the deposited wall. The errors in predicting W_E are higher than the errors for other bead geometries, because high power input and double wire feeding complicated the deposition process, causing an unsymmetric shape of deposited beads (Fig. 11d). This shape implies that there is an increased deviation of the assumed shape symmetry in the model from the reality, and it can also cause uncertainty in experimental measurement of the W_E. The results show that the average total error for W_E, $W_{Max.}$ and h_l are 22.5 %, 5.0 % and 4.7 %, respectively, of which the errors for $W_{Max.}$ and h_l are below 10 % in nineteen cases.

4.2. Process parameters predictions

The w-DED experiments of the PTA and CW-GMA processes were also used to validate the reverse model for the prediction of process parameters. In this backward algorithm, the material properties and bead geometries ($W_{Max.}$ and h_l) were given as inputs, while the process parameters such as travel speed S, current I, and voltage V were calculated as outputs. Although either maximum wall width or effective wall width can be used as one input, the former was chosen in this study since the model prediction error for the latter was higher for the CW-GMA process (Section 4.1.2). It should be noted that S_w was also prescribed in the algorithm as an input to make a balance between the unknown variables and the governing equations. The process parameters were calculated using the average measured bead geometries in three different cross sections of the deposited wall, while the error bars in

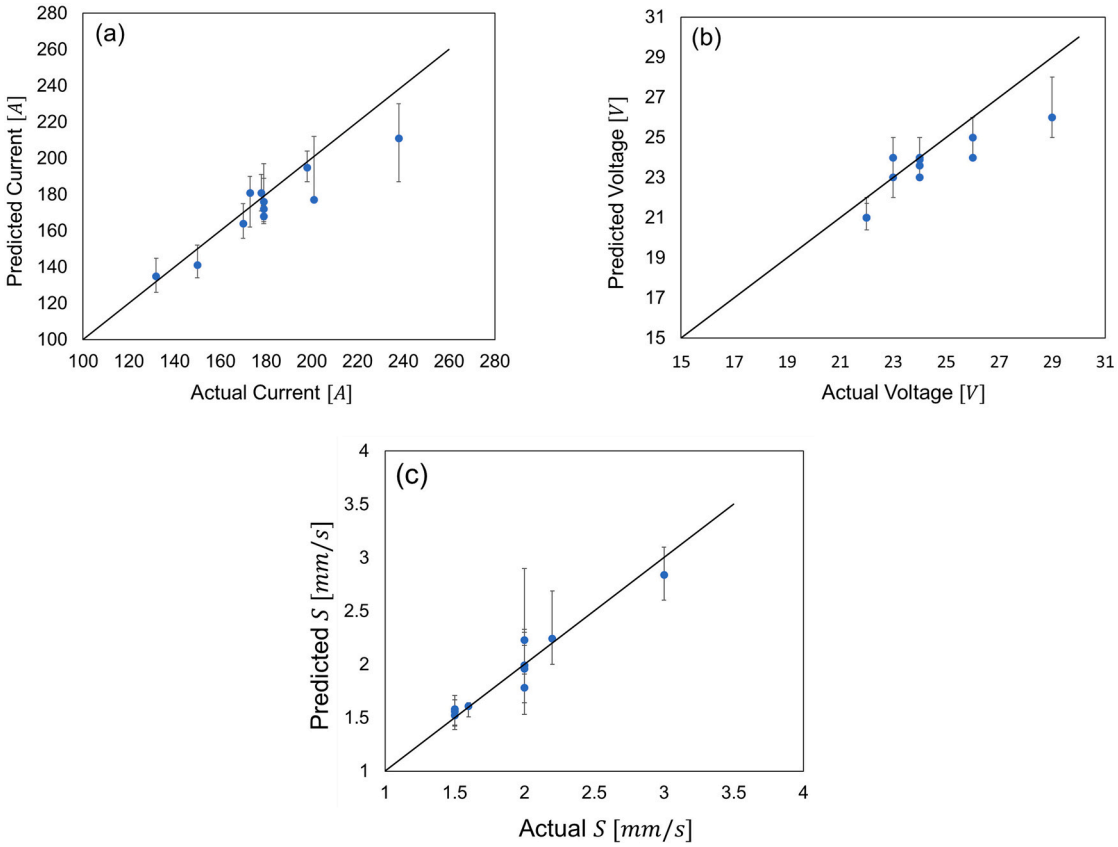

Fig. 12. Comparison of predicted and actual arc current I (a), voltage V (b) and travel speed S (c) for the PTA deposition process with an inter-layer temperature of 70 °C.

following figures correspond to the extreme calculated process parameters for each sample in different cross sections.

4.2.1. Predicted PTA process parameters

Fig. 12a–c shows the comparison of the predicted and actual process parameters in eleven cases of the PTA process at the inter-layer temperature of 70 °C. Again, the solid line indicates an ideal situation where the predicted and actual parameters are equal. So, the vertical distance of each data point from the solid line is the magnitude of the prediction error for that case. It is clearly seen that the model achieved good prediction accuracy.

4.2.2. Predicted CW-GMA process parameters

In the reverse model of CW-GMA process, the total wire feed speed was used as one input, while the individual feed speeds for the hot and cold wires were two outputs. From Fig. 13a–e and Table 3, it is found that the total average errors of the predicted arc current, voltage, travel speed, hot and cold wire feed speeds are 3.6 %, 2.2 %, 6.0 %, 4.1 % and 6.3 %, respectively, with consideration of the average and extreme dimensions of the deposit bead in different cross sections. The average calculation time was 7 s. The challenges of modelling the CW-GMA process compared to other types of w-DED processes are the high power input and double wire feeding, which increase molten material and cause instability and unsymmetrical shape of the deposited bead.

It is interesting to see that the reverse model can achieve reasonable predictions for the complicated CW-GMA process. This is probably because the consumed power for each wire is correctly calculated by considering wire specifications such as the thermal properties and S_w. The discrepancy between the prediction and measurement can be attributed to both the difficulty in experimental measurement and the limitation of the model. The uncertainty in measuring the geometries of CW-GMA deposit beads could be high because the deposited walls, in most cases, are not symmetric and have a rough surface. The model assumes ideal symmetric bead shape which is difficult to achieve using the CW-GMA process.

5. Conclusions

A thermo-capillary-gravity bidirectional analytical model was developed to predict bead geometries in the forward direction and estimate process parameters in the backward direction. A new method for determining the power transfer and wire melting efficiencies, as well as the calibration of penetration melting efficiency, was also proposed. This analytical model is based on the fundamental physical laws, making it robust, accurate and adaptable. The specification and execution of the model is also efficient: the experimental calibration of the empirical efficiency parameters only needs about six samples, and in most cases seven Newton-Raphson iterations are needed for solving the governing equations. Moreover, both forward and reverse algorithms are applicable to different w-DED processes and materials.

The analytical model has been validated for two w-DED variants including PTA and CW-GMA deposition processes. The model predictions showed good agreement with experimental measurements. On one hand, the average percentage error of the predicted bead geometries, such as maximum wall width and layer height for the PTA process with single wire feeding, was below 9.8 %. For the CW-GMA process with complicated double wire feeding, the predicted effective wall width encountered a higher error compared to other bead geometries, due to the asymmetric shape of the deposited beads, which deviated from the model assumption and increased the experimental measurement uncertainty. On the other hand, the predicted arc current, voltage and travel speed (and the CW-GMA cold and hot wire feed speeds) for

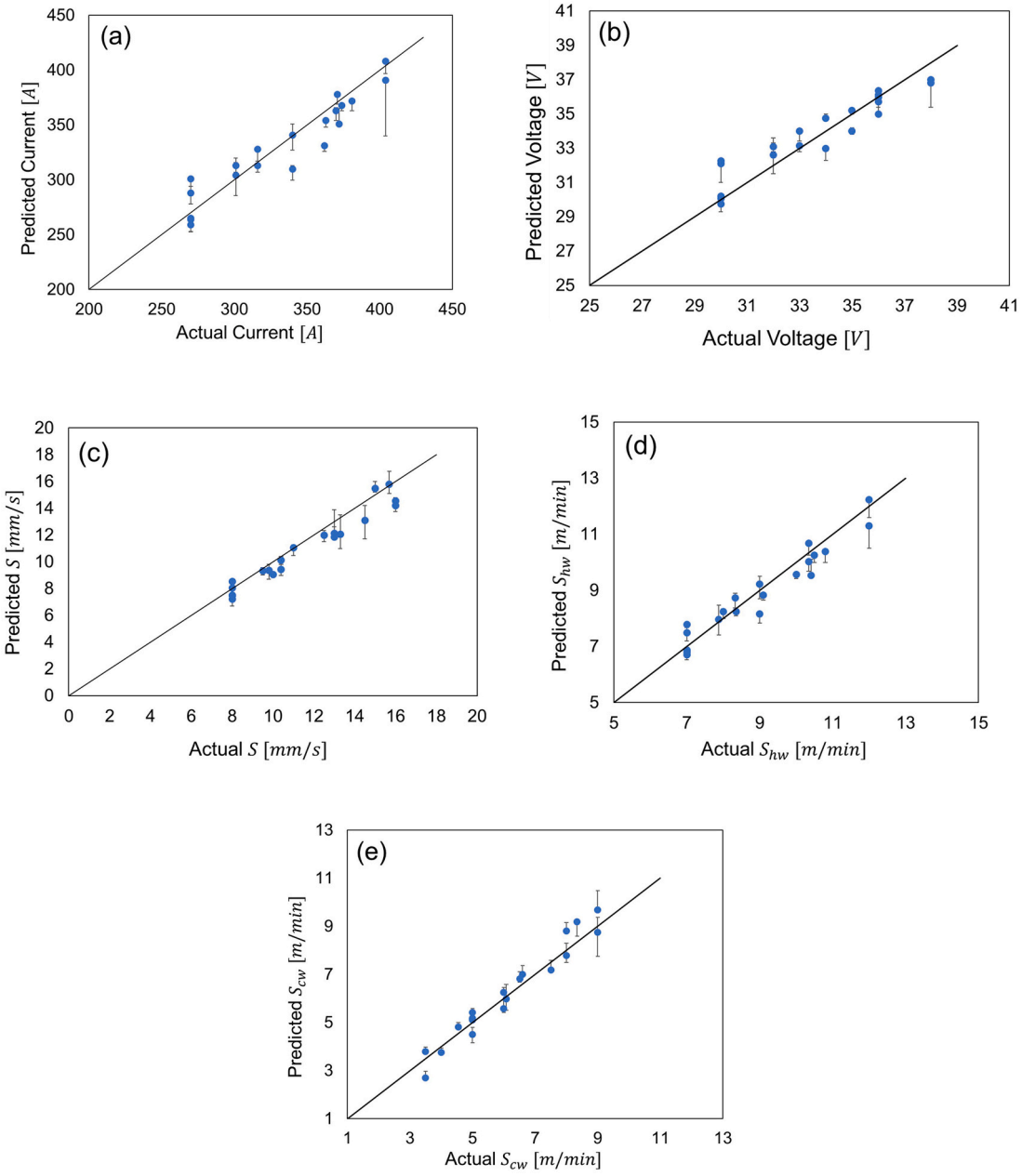

Fig. 13. Comparison of predicted and actual arc current I (a), voltage V (b), travel speed S (c), hot wire feed speed S_{hw} (d) and cold wire feed speed S_{cw} (e) for the CW-GMA deposition process with an inter-layer temperature of 70 °C.

Table 3
Average, Min. and Max. errors of predicted CW-GMA process parameters

Process Parameter	Average Err. for all samples %	Min Err. %	Max. Err. %
I [A]	3.6	0.3	10.3
V [V]	2.2	0.1	7.0
S [mm/s]	6.0	0.5	11.2
S_{hw} [m/min]	4.1	1.1	10.0
S_{cw} [m/min]	6.3	1.5	22.6

the single-pass deposition of steel wall using the PTA and CW-GMA processes had errors below 4.9 % and 6.3 %, respectively. The bidirectional analytical model would help understand the role of fundamental physical laws in determining w-DED process attributes, saving time and cost through predicting bead profiles and process parameters in the evaluation and design of additive manufacturing.

Declaration of competing interest

The authors declare that they have no known competing financial interests or personal relationships that could have appeared to influence the work reported in this paper.

Data availability

Data underlying this study can be accessed through the Cranfield University repository at https://doi.org/10.17862/cranfield.rd.24118740

Acknowledgements

Alireza M. Haghighi would like to express his gratitude to Cranfield University and EPSRC for supporting his PhD research. The authors also

would like to thank John Thrower, Mark Allen, Flemming Nielsen and Nisar Shah for their technical support. The funding by the NEWAM programme (EP/R027218/1) is also gratefully acknowledged.

References

[1] Aldalur E, Veiga F, Suárez A, Bilbao J, Lamikiz A. Analysis of the wall geometry with different strategies for high deposition wire arc additive manufacturing of mild steel. Metals (Basel) 2020;10:1–19. https://doi.org/10.3390/met10070892.
[2] Jia C, Liu W, Chen M, Guo M, Wu S, Wu C. Investigation on arc plasma, droplet, and molten pool behaviours in compulsively constricted WAAM. Addit Manuf 2020;34:101235. https://doi.org/10.1016/j.addma.2020.101235.
[3] Wang C, Suder W, Ding J, Williams S. The effect of wire size on high deposition rate wire and plasma arc additive manufacture of Ti-6Al-4V. J Mater Process Technol 2021;288:116842. https://doi.org/10.1016/j.jmatprotec.2020.116842.
[4] Lee HK, Kim J, Pyo C, Kim J. Evaluation of bead geometry for aluminum parts fabricated using additive manufacturing-based wire-arc welding. Processes 2020;8:1–14. https://doi.org/10.3390/pr8101211.
[5] Chaturvedi M, Scutelnicu E, Rusu CC, Mistodie LR, Mihailescu D, Arungalai Vendan S. Wire arc additive manufacturing: review on recent findings and challenges in industrial applications and materials characterization. Metals 2021;11:6. https://doi.org/10.3390/met11060939.
[6] Wang C, Bai H, Ren C, Fang X, Lu B. A comprehensive prediction model of bead geometry in wire and arc additive manufacturing. J Phys Conf Ser 2020;1624:2. https://doi.org/10.1088/1742-6596/1624/2/022018.
[7] Ahsan MRU, Seo GJ, Fan X, Liaw PK, Motaman S, Haase C, et al. Effects of process parameters on bead shape, microstructure, and mechanical properties in wire + arc additive manufacturing of Al0.1CoCrFeNi high-entropy alloy. J Manuf Process 2021;68:1314–27. https://doi.org/10.1016/j.jmapro.2021.06.047.
[8] Cadiou S, Courtois M, Carin M, Berckmans W, Le Masson P. Heat transfer, fluid flow and electromagnetic model of droplets generation and melt pool behaviour for wire arc additive manufacturing. Int J Heat Mass Transf 2020;148:119102. https://doi.org/10.1016/j.ijheatmasstransfer.2019.119102.
[9] Bai X, Colegrove P, Ding J, Zhou X, Diao C, Bridgeman P, et al. Numerical analysis of heat transfer and fluid flow in multilayer deposition of PAW-based wire and arc additive manufacturing. Int J Heat Mass Transf 2018;124:504–16. https://doi.org/10.1016/j.ijheatmasstransfer.2018.03.085.
[10] Lu X, Cervera M, Chiumenti M, Li J, Ji X, Zhang G, et al. Modeling of the effect of the building strategy on the thermomechanical response of Ti-6Al-4V rectangular parts manufactured by laser directed energy deposition. Metals 2020;10(12):1643. https://doi.org/10.3390/met10121643.
[11] Li L, Zhang X, Cui W, Liou F, Deng W, Li W. Temperature and residual stress distribution of FGM parts by DED process: modeling and experimental validation. Int J Adv Manuf Technol 2020;109:451–62. https://doi.org/10.1007/s00170-020-05673-4.
[12] Hackenhaar W, Mazzaferro JAE, Montevecchi F, Campatelli G. An experimental-numerical study of active cooling in wire arc additive manufacturing. J Manuf Process 2020;52:58–65. https://doi.org/10.1016/j.jmapro.2020.01.051.
[13] Ríos S, Colegrove PA, Martina F, Williams SW. Analytical process model for wire + arc additive manufacturing. Addit Manuf 2018;21:651–7. https://doi.org/10.1016/j.addma.2018.04.003.
[14] Sarathchandra DT, Davidson MJ, Visvanathan G. Parameters effect on SS304 beads deposited by wire arc additive manufacturing. Mater Manuf Process 2020;35:852–8. https://doi.org/10.1080/10426914.2020.1743852.
[15] Xia C, Pan Z, Zhang S, Polden J, Wang L, Li H, et al. Model predictive control of layer width in wire arc additive manufacturing. J Manuf Process 2020;58:179–86. https://doi.org/10.1016/j.jmapro.2020.07.060.
[16] Mbodj NG, Abuabiah M, Plapper P, El Kandaoui M, Yaacoubi S. Bead geometry prediction in laser-wire additive manufacturing process using machine learning: case of study. Appl Sci 2021;11:11949. https://doi.org/10.3390/app112411949.
[17] Geng R, Du J, Wei Z, Xu S, Ma N. Modelling and experimental observation of the deposition geometry and microstructure evolution of aluminum alloy fabricated by wire-arc additive manufacturing. J Manuf Process 2020;64:369–78. https://doi.org/10.1016/j.jmapro.2021.01.037.
[18] Bock FE, Herrnring J, Froend M, Enz J, Kashaev N, Klusemann B. Experimental and numerical thermo-mechanical analysis of wire-based laser metal deposition of Al-Mg alloys. J Manuf Process 2021;64:982–95. https://doi.org/10.1016/j.jmapro.2021.02.016.
[19] Matsunawa Akira, Takayoshi OH. Role of surface tension in fusion welding (part 1). Trans JWRI 1982;11(2):145–54. http://hdl.handle.net/11094/5800.
[20] Mohebbi MS, Kühl M, Ploshikhin V. A thermo-capillary-gravity model for geometrical analysis of single-bead wire and arc additive manufacturing (WAAM). Int J Adv Manuf Technol 2020;109:877–91. https://doi.org/10.1007/s00170-020-05647-6.
[21] Gennes PG, Brochard-Wyart F, Quéré D. Capillarity and wetting phenomena: drops, bubbles, pearls, waves. New York: Springer; 2004. p. 7–9.
[22] Hernández Paricio LJ. Bivariate Newton-Raphson method and toroidal attraction basins. Numer Algorithms 2016;71:349–81. https://doi.org/10.1007/s11075-015-9996-3.
[23] Kim IS, Kwon WH, Siores E. An investigation of a mathematical model for predicting weld bead geometry. Can Metall Quart 1996;35(4):385–92. https://doi.org/10.1016/S0008-4433(96)00012-2.
[24] Lee JI, Um KW. Prediction of welding process parameters by prediction of back-bead geometry. J Mater Process Technol 2000;108:106–13. https://doi.org/10.1016/S0924-0136(00)00736-6.
[25] Karmuhilan M, Sood AK. Intelligent process model for bead geometry prediction in WAAM. Mater Today Proc 2018;5:24005–13. https://doi.org/10.1016/j.matpr.2018.10.193.
[26] Wang Chong, Wang Jun, Bento João, Ding Jialuo, Pardal Goncalo, Chen Guangyu, et al. A novel cold wire gas metal arc (CW-GMA) process for high productivity additive manufacturing. Addit Manuf 2023;73:103681. https://doi.org/10.1016/j.addma.2023.103681.
[27] Kou S. Welding metallurgy. New Jersey, USA431(446); 2003. p. 223–5.
[28] Dupont JN, Marder AR. Thermal efficiency of arc welding processes. Weld J 1995;74(12):406–16.
[29] Barrionuevo GO, Sequeira-Almeida PM, Ríos S, et al. A machine learning approach for the prediction of melting efficiency in wire arc additive manufacturing. Int J Adv Manuf Technol 2022;120:3123–33. https://doi.org/10.1007/s00170-022-08966-y.